On the reaction mechanism of MnOx/SAPO-34 bifunctional catalysts for the conversion of syngas to light olefins

C. Coudercy, V. L'Hospital, R. Checa, A. Le Valant, P. Afanasiev, S. Loridant

On the reaction mechanism of MnOx/SAPO-34 bifunctional catalysts for the conversion of syngas to light olefins

Christophe Coudercy,[a] Valentin L'hospital,[b] Ruben Checa,[a] Anthony Le Valant, [b] Pavel Afanasiev [a] and Stéphane Loridant[a,*]

MnO_x/SAPO-34 bifunctional catalysts are efficient for the conversion of syngas to light olefins. However, the reaction mechanism is still debated in particular the nature of the intermediate formed on MnO_x (ketene vs methanol). In this study, it was evidenced from catalytic data and *in situ* DRIFT measurements that methanol is a key reaction intermediate produced on MnOx that synergistically reacts with SAPO-34 to produce light olefins.

Light olefins (C_2–C_4) are key building-block chemicals to produce plastics, medicines and paints. They are presently produced worldwide in huge amounts (exceeding 150 $Mt.y^{-1}$) mostly by steam cracking of naphta which is highly energy-consuming process. Alternative eco-efficient processes such as oxidative dehydrogenation of light alkanes, dehydration of bio-alcohols are attractive, but the former suffers from both low selectivity at high conversion and process limitations[1] and the latter from both insufficient catalyst stability and costly lignocellulose biorefineries.[2-5]

Syngas-based processes will become more attractive in the future since renewable carbon resources (biomass, wastes, CO_2) are expected to gradually replace fossil fuels.[6] A two-step process including methanol synthesis followed by methanol-to-olefins (MTO) process is commercially available to produce light olefins but development of a more energetically and costly-efficient direct process is needed.[7] In spite of important progresses, the direct Fischer-Tropsch to Olefins (FTO) process is limited by the Anderson−Schultz− Flory (ASF) distribution and the maximal selectivity to C2-C4 hydrocarbons is around 60%.[6-9]

Few years ago, a composite catalyst obtained by physically mixing a reducible metal oxide ($ZnCrO_x$) and a zeotype (MSAPO) enabled direct conversion of syngas to light olefins giving a selectivity to light olefins (excluding CO_2) as high as 80% at a CO conversion of 17%, well-surpassing the limit predicted by the ASF distribution model via the FTO route.[8,9] This combination of an oxide and a zeotype was called OXZEO by Jiao et al.[8] A high selectivity to light olefins (74%) at a conversion of 11% was reported the same year using ZnZrOx oxide instead of $ZnCrO_x$ and

different reaction conditions.[10] Since then, numerous other metal oxide−zeotype combinations yielding a high selectivity to light olefins have been reported and this concept was recently reviewed.[7,9] It is designed in the literature either by OXZEO or more generally by STO (syngas to olefins). Most of oxides contained Zn: ZnO,[11] $ZnCrO_x$,[8,12-19] $ZnZrO_x$,[10,20,21] $ZnAlO_x$,[22-24] Zr-promoted $ZnAlO_x$,[25] La-doped $ZnAlO_x$,[26] Zn spinels,[27] $ZnCeZrO_x$.[28-31] Alternatively, MnO_x,[32] $MnGaO_x$,[33,34] or $ZrInO_x$,[35] was used. The zeotype corresponded most of the time to SAPO-34 (microporous, microsized) or to mesoporous M-SAPO,[8,11,32] hierarchical SAPO-34,[21] nanosized SAPO-34,[12,25] SAPO-18,[13,18] SAPO-35,[18] various SAPOs,[24] AlPO-18,[36] SSZ-13,[17,20]. Finally, note that a 1000 $t.y^{-1}$ industrial pilot plant was built in Shaanxi, China.[9]

The reaction mechanism leading to light olefins is still debated:[7,9] on one hand, the Xinhe Bao's group proposed that CO is activated through the Boudouard reaction (disproportionation to CO_2 and adsorbed C*) on reduced metal oxide surfaces. CH_2 species are formed by direct reaction of C* with H_2 and then react with CO to produce CH_2CO (i.e. ketene) as an intermediate,[8,9,32,33] which subsequently diffuses into the zeotype to form lower olefins by C-C coupling.[9,37] CH_4 is formed by reaction of CH_2 species and H_2. On the other hand, methanol and dimethyl ether (DME) formation in significant amounts was evidenced over ZnO,[10] $ZnZrO_x$,[10,20] $ZnAlO_x$,[22,23], Zn spinels[27] and $ZrInO_x$[35] In this case, non-dissociative activation of CO leads to formates and methoxy species as shown by *in situ* DRIFT measurements.[20,27,31] Light olefins are then produced over the zeotype similarly to the MTO process and methane arises from consecutive methanol decomposition by C-O cleavage on oxygen vacancies.[35] Therefore, further studies on the reaction mechanism are needed. Anyway, the key intermediates (ketene versus methanol) may vary with metal oxides and reaction conditions[9] and both mechanisms could occur in parallel.[38]

As regards MnOx/SAPO-34 bifunctional catalysts, ketene was assumed to be the key intermediate[32] by analogy with $ZnCrO_x$[8] and possibly because the selectivity to methanol and DME was lower than 0.5% in the reaction conditions. Note that MnOx tested alone led to ca 50% of methane which is much higher than when SAPO-34 is added.[32] *In situ* DRIFT measurements achieved at room temperature (RT) on MnO after pre-treatments (H_2 or N_2) at various temperatures and adsorption of CO at RT revealed formation of carbonates. The characteristic □(C−H) stretching bands of formate species typically at 2840−2845 and 2945−2950 cm^{-1} were not observed.[32]

In this paper, a new insight into the reaction mechanism of MnO_x/SAPO-34 bifunctional catalysts is provided from catalytic performances and *in situ* DRIFT measurements achieved on MnOx alone and on MnO_x/SAPO-34 mechanical mixtures.

As in the reference study,[32] MnO_x was obtained from $MnCO_3$ (see details in the Supporting Information). Its BET surface area was 23 $m^2.g^{-1}$. A single MnO manganosite phase with a crystallite size of 21 nm was evidenced from XRD (Fig. S1). Its However, Raman spectroscopy revealed the presence of Mn_3O_4 (bands at 318, 370 and 656 cm^{-1})[39-41] in addition to MnO feature around 550 cm^{-1}.[42-44] Mn_3O_4 is probably present as an amorphous or nanocrystalline overlayer[45] formed upon exposure to air at RT. Mn_3O_4 becomes more crystallized upon increasing the temperature to 360 °C under 10%H_2-N_2 flow (thinner bands in Fig. S2) before disappearing at higher temperatures. Then, the spectra contained mainly two broad bands at 546 and 626 cm^{-1}. The former was attributed to the 2TO (Transverse Optical) or LO (Longitudinal Optical) mode of MnO[42-44] while the other one is not observed for single crystals. Its observation could be related to the nanocrystallinity and/or non-stoichiometry ($MnO_{1\pm\square}$ $\square$. Furthermore, the IR bands at 3680, 3630 cm^{-1} and 863 cm^{-1} observed in the *in situ* DRIFT spectra of MnO_x under H_2 flow between 380 and 450 °C (Fig. S3) were attributed to surface hydroxyl[46] and carbonated species,[47-48] respectively. Activation of MnO_x under H_2 flow at 410 °C enabled to absorb CO at -2 °C as revealed by observation of IR bands at 2062, 2038, 1984, 1962, 1927 and 1917 cm^{-1} (Fig. S4) corresponding to $Mn_y(CO)_x$ species.[49-51] However, no adsorption was evidenced after activation under He at the same temperatures showing that the Mn_3O_4 passivation layer does not adsorb CO. It was concluded that reduction of Mn_3O_4 leads to formation of oxygen vacancies at the surface of MnO_x able to adsorb CO. Note that no signals corresponding to linearly absorbed CO were previously observed on both fresh sample and those reduced at different temperatures.[32]

As shown in Table 1, MnO_x activated under H_2 led to a CO conversion of 2.5% with a high selectivity (>30%) to CO_2 and CH_4. Interestingly, a significant selectivity to CH_3OH (8.1%) was determined. The other by-products were C2+ hydrocarbons with an O/P (olefins to paraffins) ratio of 1.47 and traces of DME.

SAPO-34 was synthetized by a hydrothermal method (see details in the SI) and a microcrystalline powder was obtained after calcination (see XRD diagram in Fig. S5 and SEM image in Fig. S6). Its framework composition was Si/Al/P:0.14/1/0.66. The solid was mostly microporous since its BET surface area was 461 $m^2.g^{-1}$ while the microporous one was 397 $m^2.g^{-1}$, the difference between the two values (64 $m^2.g^{-1}$) corresponding to the mesoporous one due to intergranular porosity. Its microporous volume was 0.19 $cm^3.g^{-1}$.

The catalytic tests were carried out using different arrangements of SAPO-34 and MnO_x layers in a catalytic bed (see details in the SI and Table.S1), in order to vary the degree of contact between the two functions. In the separated double layer (SDL), the layers of MnOx and SAPO-34 were

separated by a SiC inert layer, so the interaction between the two phases was the smallest. Then the contact progressively increased in the simple double layer (DL), triple layer (MLx3) and quadruple layer (MLx4) bed.

Table 1 Catalytic data obtained for MnO_x, MnO_x/SAPO-34 separated double layer (SDL), double layer (DL) and Multi-Layer (ML) catalytic beds. Reaction conditions: m(MnOx)=600 mg, m(SAPO-34)=300 g, P=25 bar, T=410 °C, H_2/CO/Ar=63.8/25.6/10.6, WHSV=87 $mL.min^{-1}.g^{-1}$.

			Selectivity value (%)											
Sample	X_{CO}(%)[a]	O/P[b]	CO_2	CH_4	CH_3OH	DME	C2=	C2	C3=	C3	C4=	C4	C5=	C5
MnOx	2.5	1.47	32.8	37.8	8.1	0.5	4.1	4.8	2.9	1.9	5.0	0.7	0.5	1.1
SDL	2.6	1.66	34.5	32.3	1.2	0	6.7	5.7	6.6	4.5	6.4	1.7	0.4	0.2
DL	3.3	1.33	38.1	24.4	0.9	0	7.3	5.9	8.1	7.3	5.6	2.1	0.3	0.2
MLx3	4.6	2.04	37.4	18.5	2.3	5.4	9.5	4.4	10.2	5.0	4.5	2.0	0.3	0.6
MLx4	4.7	1.31	37.8	18.5	0.8	0	8.3	6.5	11.5	8.8	4.2	2.9	0.3	0.3

[a]: CO conversion,

[b]: olefins to paraffins molar ratio.

Addition of SAPO-34 to MnO_x as a separated double layer (see SDL in Table 1) led to a drastic decrease in the CH_3OH selectivity (and to a lesser extent, in the CH_4 one) while the selectivity to C2+ hydrocarbons and the O/P ratio were significantly increased. This trend was emphasized increasing proximity between MnO_x and SAPO-34 as shown by the data obtained for double layer and multi-layer catalytic beds (DL, MLx3, MLx4 in Table 1). Furthermore, the CO conversion increased which can be explained by a synergistic effect between MnO_x and SAPO-34. The slight increase in the CO_2 selectivity could arise from production of higher amount of H_2O favouring the water-gas shift reaction. The decrease in the CH_4 selectivity agrees with a limitation of consecutive hydrogenation of CH_3OH[35] over MnO_x when SAPO-34 is available to transform CH_3OH into C2+ hydrocarbons. Note that the decrease in the O/P ratio was due to the increase in CO conversion as paraffins are consecutively produced from olefins by hydrogenation.[32] Interestingly, the presence of an additional MnO_x layer in the lower part of the catalytic bed led to much higher amounts of DME and CH_3OH (compared MLx3 and DL in Table 1) confirming these compounds are reaction intermediates.

The catalytic properties of MnO_x/SAPO-34 mechanical mixtures were also determined and the influence of SAPO-34 addition was investigated for its variable proportion. No significant difference of catalytic performances was observed activating the catalysts under H_2 flow from 410 to 450 °C (Fig. S7). For these measurements, CH_3OH and DME were not analyzed as their amounts were assumed to be low.[32] The reaction conditions were similar in spite of a lower H_2/CO ratio (2.0 instead of 2.5). Again, a low CO conversion was obtained with MnO_x alone and the main products were CH_4 and CO_2. The CO conversion linearly increased (Fig. S8a) with the contact time while the selectivity values remained unchanged (Fig. S8b). However, the O/P ratio decreased increasing the CO conversion (Fig. S8a) indicating that paraffins were consecutively formed from olefins.

As shown in Fig. 1, addition of only 5% of SAPO-34 strongly increased the CO conversion and drastically increased the C2-C4 selectivity at the expense of CH_4 whereas the CO_2 selectivity remained similar.

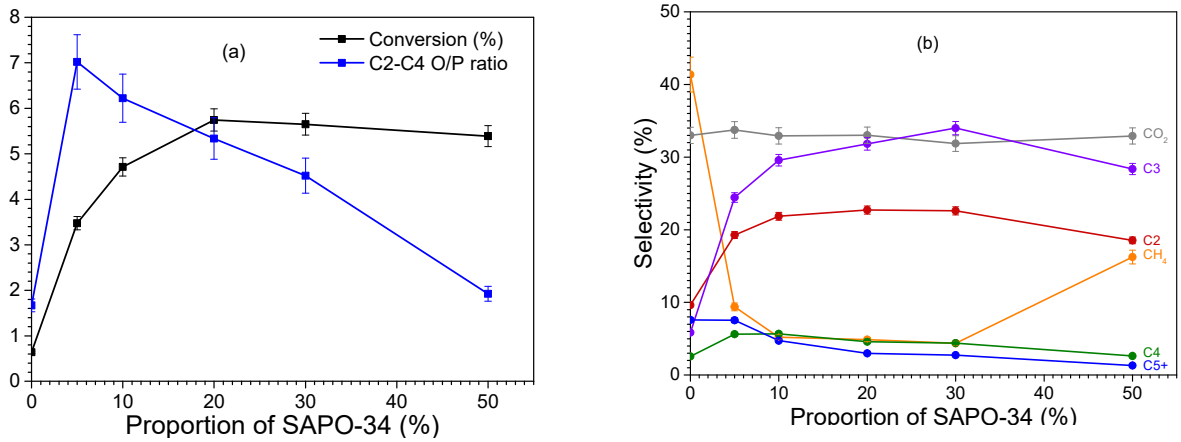

Fig.1 (a) Evolution of the conversion and the C2-C4 O/P ratio and (b) Evolution of the selectivity values with the proportion of SAPO-34. Reaction conditions: m(MnOx+SAPO-34)=300 mg, P=25 bar, T=410 °C, $H_2/CO/Ar$=60/30/10, WHSV=87mL.min^{-1}.g^{-1}.

It suggests that all these products are formed from the same reaction intermediate via two competitive routes. These trends were confirmed upon increasing the proportion of SAPO-34 up to 20-30%, but the values were almost constant for higher zeotype amounts. Interestingly, an optimal O/P ratio of 7 was obtained for 5% of SAPO-34 suggesting that, as the hydrogenation properties of MnOx, the acidity of the zeotype plays a significant role in the consecutive hydrogenation of olefins.[13,21,27]

The evolution of *in situ* DRIFT spectra recorded over time at -2 °C under 20 mL.min^{-1} of 2.5%CO-He flow is plotted in Fig.2: the bands corresponding to $Mn_x(CO)_y$ species were observed immediately and they increased for the first 12 min before being strongly decreased afterwards. At the same time, additional bands rose between 900-1100 cm^{-1} and 1200-1700 cm^{-1}. Those bands were attributed to □$_1$ and □$_3$ vibrations, respectively of monodentate, chelating bridging and bridging bidentate carbonates.[47] Note that the splitting of the degenerate □$_3$ vibration (E mode for free carbonate with D_{3h} symmetry) is typical of each species and that the □$_1$ vibration is slightly IR active due to the loss of symmetry compared to D_{3h}.[47] The intensity of carbonate bands continued to grow after 12 min when $Mn_x(CO)_y$ species began to disappear. Formation of carbonates species over activated MnO_x was already reported by Zhu et al. and attributed to the Boudouart reaction.[32] Note that this exothermic reaction is thermodynamically favorable but could be kinetically limited at -2 °C. Alternatively, it would imply a redox mechanism during which lattice oxygen is consumed to form carbonates and electrons ($CO + 2O^{2-} \rightarrow CO_3^{2-} + 2e^-$) leading to reduction of MnO_x. Finally, it was confirmed that carbonates are stable[32] since they were still observed flowing He at 200 °C.

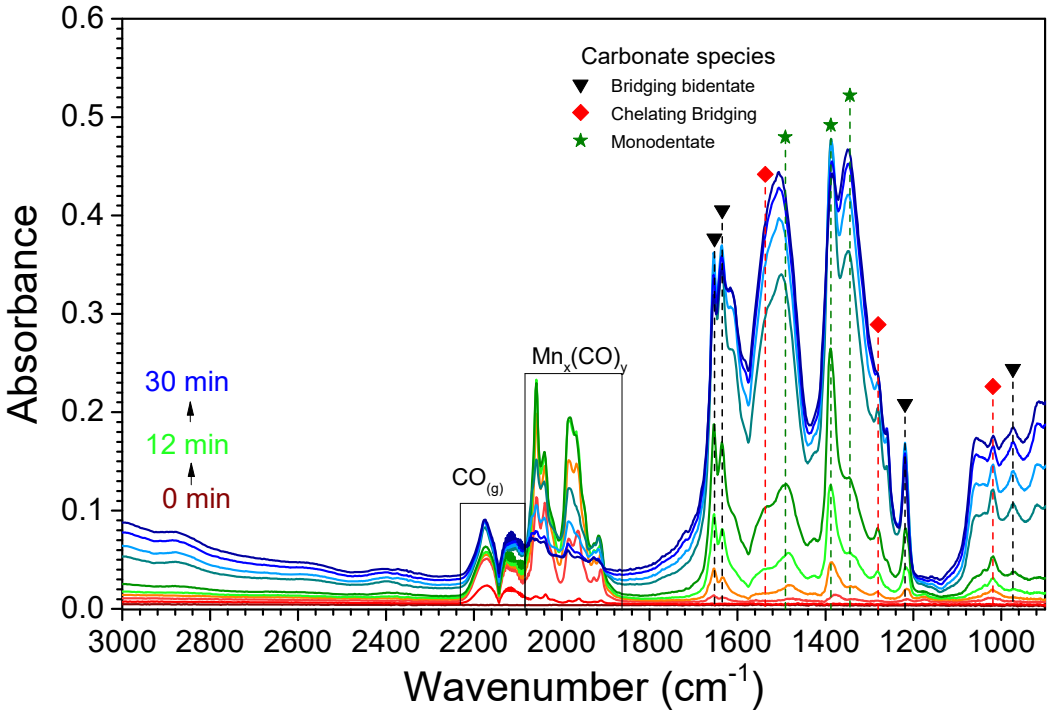

Fig.2 *In situ* DRIFT spectra of MnO_x sample recorded over time for 30 min at -2 °C under 20 mL.min^{-1} of 2.5%CO-He flow. The background corresponded to the spectrum recorded under 20 mL.min^{-1} of He flow at -2 °C after activation at 430 °C under 20 mL.min^{-1} H_2 flow for 30 min.

Furthermore, we carried out *in situ* DRIFT experiments under H_2/CO flow at the reaction temperature. The spectral evolution of MnO_x sample recorded over time at 410 °C under 20 mL.min^{-1} of 2.5%CO/7.5%H_2/90%He flow is plotted in Fig. 3: some bands typical of formate species were

unambiguously observed at 2820 and 2715 cm^{-1} (□(C-H) and □$_s$(O-C-O)+□(C-H), respectively).[52-54] These formate bands rose for 10 min and then remained constant. Furthermore, bands observed around 2143 and 2349 cm^{-1} were attributed to CO and CO_2 molecules in the gas phase, respectively.[48,55] As for CO adsorption at -2 °C, numerous bands were observed at 1700-1200 cm^{-1}. They could either be attributed to formates,[52-54] or to carbonates.[47] Furthermore, the bands at 1060, 988 cm^{-1} could also correspond to these species as well as methoxy ones.[56-58] However, as all these bands evolved with the same rate as the bands at 2820 and 2715 cm^{-1}, they were attributed to formates. In particular, the bands at 1651 and 1614 corresponded to □$_{as}$(O-C-O) vibrations, the ones at 1384, 1353 cm^{-1} to □$_s$(O-C-O) and □(OC-H) and the ones at 1060, 988 cm^{-1} to □(OC-H).[59] Formate species have been reported as intermediates leading to methanol formation.[20,27,31] However, the □$_{as}$(CH_3) band at 2900-2900 cm^{-1} [56-58] typical of methoxy species was not observed in the DRIFT spectra. This feature was explained by a slower formation rate of methoxy species from formates compared to the formation rate of formates and methanol [7]

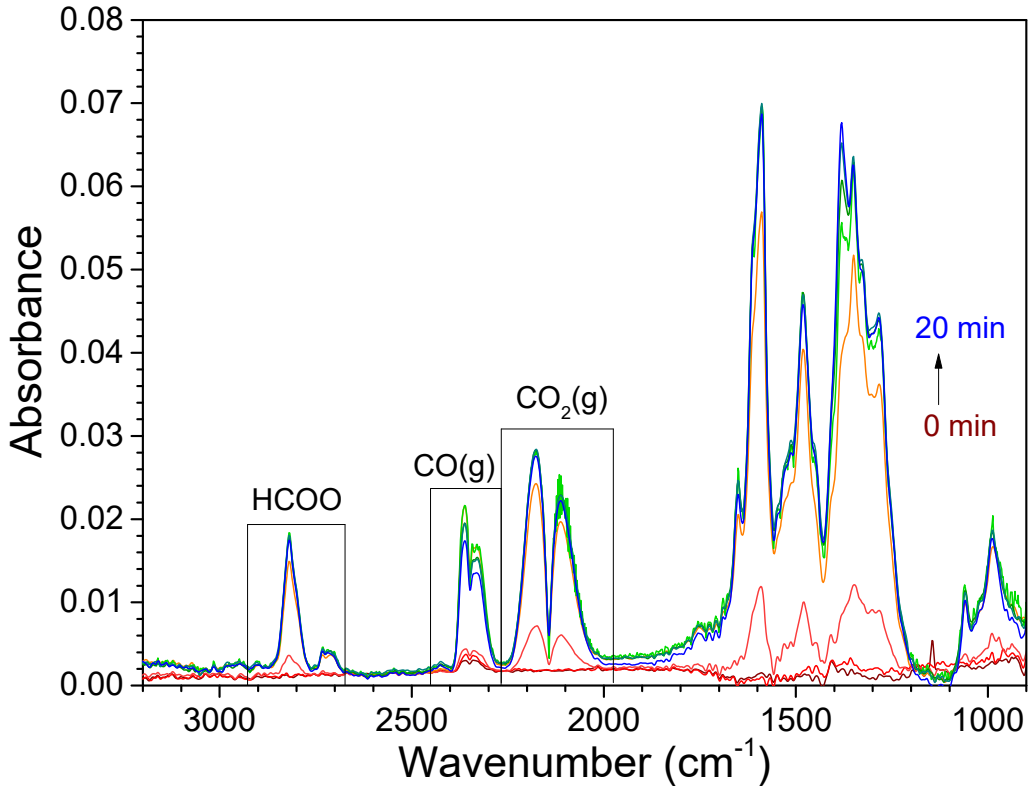

Fig.3 *In situ* DRIFT spectra of MnO_x sample recorded over time at 410 °C under 20 $mL.min^{-1}$ of 2.5%CO/7.5%H_2/90%He flow. The background corresponded to the spectrum recorded under 20 $mL.min^{-1}$ of He flow at 410 °C after activation at 430 °C under 20 $mL.min^{-1}$ H_2 flow for 30 min.

Addition of only 10% wt. of SAPO-34 to MnO_x led to a drop of absorbance of formates bands by 2 times whereas after addition of 25% wt. of SAPO-34, the formates bands became by 4 times less intense (Fig.4). This evidenced a strong decrease of the steady state concentration of formate species caused by addition of zeotype, probably due to methanol conversion over SAPO-34. For the 75%MnO_x-25%SAPO-34 sample, formates were re-stabilized after decreasing the temperature down to 250 °C (Fig. S9) which was due to the lowering of catalytic activity.

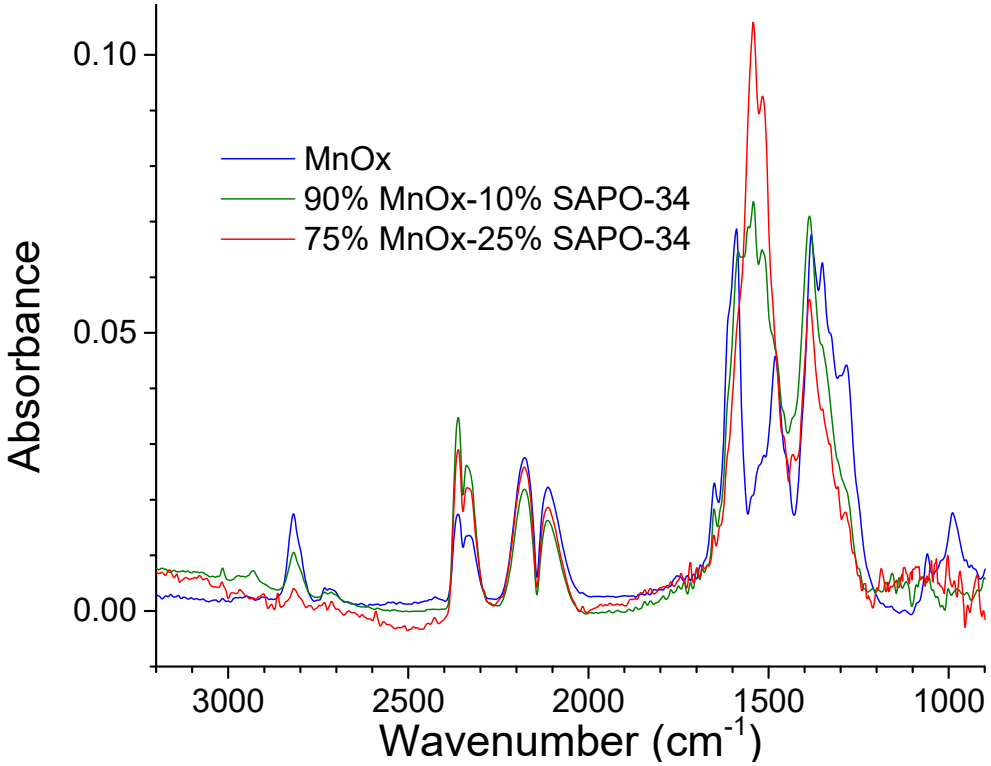

Fig.4 *In situ* DRIFT spectra of MnO_x, 90%MnO_x-10%SAPO-34 and 75%MnO_x-25%SAPO-34 samples recorded at 410 °C after 10 min under 20 mL.min^{-1} of 2.5%CO/7.5%H_2/90%He flow. The backgrounds corresponded to the spectra recorded under 20 mL.min^{-1} of He flow at 410 °C and activation at 430 °C under 20 mL.min^{-1} H_2 flow for 30 min.

Conclusions

In this study, the reaction of H_2/CO over MnO_x was shown to produce methanol in addition to CH_4, CO_2 and C2-C5 hydrocarbons. When SAPO-34 is present as an additional catalytic bed, methanol is converted to C2+ hydrocarbons. The CH_4 selectivity is then decreased suggesting it is formed by hydrogenation of methanol. A similar phenomenon was evidenced for MnO_x/SAPO-34 mechanical mixtures.

In situ DRIFT measurements achieved on MnO_x under CO at low temperature revealed a reactive adsorption phenomenon leading to formation of strong carbonates. Differently, *in situ* DRIFT

spectra under H_2/CO flow at the reaction temperature evidenced the presence of formates. Addition of SAPO-34 in mechanical mixture with MnO_x leads to consumption of formates in agreement with consumption of methanol over SAPO-34 to form C2+ hydrocarbons.

Therefore, we proposed that methanol is a key reaction intermediate produced on MnO_x that reacts with SAPO-34 to produce light olefins, which results in a synergistic effect between two catalytic functions.

Conflicts of interest

There are no conflicts to declare.

Acknowledgment

The French National Research agency 'Agence Nationale de la Recherche' (ANR) is acknowledged for the financial support of the INCH project (ANR-17-CE07-0011).

References

1 Gas-phase oxidation of alkanes, F. Cavani, A. Chieregato, J. M. Lopez Nieto, J.-M. M. Millet, Edited by A. J. L. Pombeiro, M. Guedes da Silva, C. Fatima Alkane Functionalization (2019), 159−188.

2 A. K. Chandel, V. K. Garlapati, A. K. Singh, F. A. Fernandes Antunes, S. S. da Silva, *Bioresour. Technol.*, 2018, **264**, 370–381.

3 V. Hulea, *ACS Catal.*, 2018, **8**, 3263–3279.

4 T. K. Phung, T. L. M. Pham, K. B. Vu, G. Busca, *J. Environ. Chem. Eng.*, 2021, **9**, 105673.

5 D. Sun, Y. Li, C. Yang, Y. Su, Y. Yamada, S. Sato, *Fuel Process. Technol.*, 2020, **197**, 106193.

6 U. Olsbye, *Angew. Chem. Int. Ed.*, 2016, **55**, 7294–7295.

7 W. Zhou, K. Cheng, J. Kang, C. Zhou, V. Subramanian, Q. Zhang, Y. Wang, *Chem. Soc. Rev.*, 2019, **48**, 3193−3228.

8 F. Jiao, J. Li, X. Pan, J. Xiao, H. Li, H. Ma, M. Wei, Y. Pan, Z. Zhou, M. Li, S. Miao, J. Li, Y. Zhu, D. Xiao, T. He, J. Yang, F. Qi, Q. Fu, X. Bao, *Science*, 2016, **351**, 1065–1068.

9 X. Pan, F. Jiao, D. Miao, X. Bao, *Chem. Rev.*, 2021, **121**, 6588−6609.

10 K. Cheng, B. Gu, X. Liu, J. Kang, Q. Zhang, Y. Wang, *Angew. Chem. Int. Ed.*, 2016, **55**, 4725–4728.

11 N. Li, F. Jiao, X. Pan, Y. Ding, J. Feng, X. Bao, *ACS Catal.*, 2019, **9**, 960–966.

12 Y. Huang, H. Ma, Z. Xu, W. Qian, H. Zhang, W. Ying, *Fuel*, 2020, **273**, 117771.

13 G. Li, F. Jiao, X. Pan, N. Li, D. Miao, L. Li, X. Bao, *ACS Catal.*, 2020, **10**, 12370−12375.

14 K. Pinkaew, G. Yang, T. Vitidsant, Y. Jin, C. Zeng, Y. Yoneyama, N. Tsubaki, *Fuel*, 2013, **111**, 727–732.

15 V. P. Santos, G. Pollefeyt, D. F. Yancey, A. Ciftci Sandikci, B. Vanchura, D.L.S. Nieskens, M. de Kok-Kleiberg, A. Kirilin, A. Chojecki, A. Malek, *J. Catal.*, 2020, **381**, 108–120.

16 L. Tan, F. Wang, P. Zhang, Y. Suzuki, Y. Wu, J. Chen, G. Yang, N. Tsubaki, *Chem. Sci.*, 2020, **11**, 4097−4105.

17 Y. Huang, H. Ma, Z. Xu, W. Qian, H. Zhang, W. Ying, *ACS Omega*, 2021, **6**, 10953−10962.

18 Y. Huang, H. Ma, Z. Xu, W. Qian, H. Zhang, W. Ying, *RSC Adv.*, 2021, **11**, 13876−13883.

19 A. V. Kirilin, J. F. Dewilde, V. Santos, A. Chojecki, K. Scieranka, A. Malek, *Ind. Eng. Chem. Res.*, 2017, **56**, 13392−13401.

20 X. Liu, W. Zhou, Y. Yang, K. Cheng, J. Kang, L. Zhang, G. Zhang, X. Min, Q. Zhang, Y. Wang, *Chem. Sci.*, 2018, **9**, 4708−4718.

21 M. Wang, Z. Wang, S. Liu, R. Gao, K. Cheng, L. Zhang, G. Zhang, X. Min, J. Kang, Q. Zhang, Y. Wang, *J. Catal.*, 2021, **394**, 181–192.

22 Y. Ni, Y. Liu, Z. Chen, M. Yang, H. Liu, Y. He, Y. Fu, W. Zhu, Z. Liu, *ACS Catal.*, 2019, **9**, 1026−1032.

23 G. Raveendra, C. Li, Y. Cheng, F. Meng, Z. Li, *New J. Chem.*, 2018, **42**, 4419–4431.

24 M. Wang, J. Kang, X. Xiong, F. Zhang, K. Cheng, Q. Zhang, Y. Wang, *Catal. Today*, 2021, **371**, 85–92.

25 G. Raveendra, C. Li, B. Liu, Y. Cheng, F. Meng, Z. Li, *Catal. Sci. Technol.*, 2018, **8**, 3527–3538.

26 G. Raveendra, B. Ma, X. Liu, Y. Guo, Y. Wang, *Catal. Sci. Technol.*, 2021, **11**, 3231–3240.

27 X. Liu, M. Wang, H. Yin, J. Hu, K. Cheng, J. Kang, Q. Zhang, Y. Wang, *ACS Catal.*, 2020, **10**, 8303−8314.

28 Y. Luo, S. Wang, S. Guo, K. Yuan, H. Wang, M. Dong, Z. Qin, W. Fan, J. Wang, *Catal. Sci. Technol.*, 2021, **11**, 338-348.

29 F. Meng, X. Li, P. Zhang, L. Yang, G. Yang, P. Ma, Z. Li, *Catal. Today*, 2021, **368**, 118–125.

30 F. Meng, X. Li, P. Zhang, L. Yang, S. Liu, Z. Li, *Appl. Surf. Sci.*, 2021, **542**, 148713.

31 S. Wang, P. Wang, D. Shi, S. He, L. Zhang, W. Yan, Z. Qin, J. Li, M. Dong, J. Wang, U. Olsbye, W. Fan, *ACS Catal.*, 2020, **10**, 2046−2059.

32 Y. Zhu, X. Pan, F. Jiao, J. Li, J. Yang, M. Ding, Y. Han, Z. Liu, X. Bao, *ACS Catal*., 2017, **7**, 2800–2804.

33 P. Zhang, F. Meng, X. Li, L. Yang, P. Ma, Z. Li, *Catal. Sci. Technol.*, 2019, **9**, 5577−5581.

34 G. Yang, F. Meng, P. Zhang, L. Yang, Z. Li, *New J. Chem.*, 2021, **45**, 7967–7976.

35 J. Su, D. Wang, Y. Wang, H. Zhou, C. Liu, S. Liu, C. Wang, W. Yang, Z. Xie, M. He, *ChemCatChem*, 2018, **10**, 1536 – 1541.

36 J. Su, H. Zhou, S. Liu, C. Wang, W. Jiao, Y. Wang, C. Liu, Y. Ye, L. Zhang, Y. Zhao, H. Liu, D. Wang, W. Yang, Z. Xie, M. He, *Nat. Commun.*, 2019, **10**, 1297.

37 C.-M. Wang, Y.-D. Wang, Z.-K. Xie, *Catal. Sci. Technol.*, 2016, **6**, 6644–6649.

38 Z.-Q. Huang, T.-H. Li, B. Yang, C.-R. Chang, *Chin. J. Catal.*, 2020, **41**, 1906–1915.

39 R. Regmi, R. Tackett, G. Lawes, *J. Magn. Magn. Mater.*, 2009, **321**, 2296–2299.

40 J. Kaczmarczyk, F. Zasada, J. Janas, P. Indyka, W. Piskorz, A. Kotarba, Z. Sojka, *ACS Catal.*, 2016, **6**, 1235−1246.

41 T. Larbi, K. Doll, T. Manoubi, J. Alloys Compd. 2016, **688**, 692–698.

42 H-h. Chou and H. Y. Fan, *Phys. Rev. B*, 1976, **13**, 3924–3938.

43 Y. Mita, Y. Sakai, D. Izaki, M. Kobayashi, S. Endo, S. Mochizuki, Phys. Stat. Sol. (b) 2001, **223**, 247–251.

44 N. Mironova-Ulmanea, A. Kuzmina, V. Skvortsovaa, G. Chikvaidzea, I. Sildosb, J. Grabisc, D. Jankovicac, A. Dindunec, M. Maiorov, Acta Phys. Pol. A, 2018, **133**, 1013–1016.

45 A. E. Berkowitz, G. F. Rodriguez, J. I. Hong, K. An, T. Hyeon, N. Agarwal, D. J. Smith, E. E. Fullerton, *J. Phys. D: Appl. Phys.* 2008, **41**, 134007.

46 A. A. Tsyganenko, V. N. Filimonov*, J. Mol. Struct.*, 1973, **19**, 579–589.

47 J. C. Lavalley, *Catal. Today* 1996, **27**, 377–401.

48 A. Goguet, F. C. Meunier, D. Tibiletti, J. P. Breen, R. Burch, *J. Phys. Chem. B*, 2004, **108**, 20240–20246.

49 G. Bor, G. Sbrignadello, *J. Chem. Soc., Dalton Trans.*, 1974, 440–448.

50 R. E. Wittrig, C. P. Kubiak*, J. Electroanal. Chem.*, 1995, **393**, 75–86.

51 D. A. Steinhurst, A. P. Baronavski, J. C. Owrutsky, *Chem. Phys. Lett.*, 2002, **361**, 513–519.

52 G. Busca, J. Lamotte, J.-C. Lavalley, V. Lorenzelli, *J. Am. Chem. Soc.*, 1987, **109**, 5197–5202.

53 C. Li, Y. Sakata, T. Arai, K. Domen, K.-I. Maruya, T. Onishi, *J. Chem. Soc., Faraday Trans. 1*, 1989, **85**, 1451–1461.

54 J. P. Durand, S. D. Senanayake, S. L. Suib, D. R. Mullins, *J. Phys. Chem. C*, 2010, **114**, 20000–20006.

55 L. Sivachandiran, F. Thevenet, A. Rousseau, *Plasma Chem Plasma Process*, 2013, **33**, 855–871.

56 M. Daturi, C. Binet, J.-C. Lavalley, A. Galtayries, R. Sporken, *Phys. Chem. Chem. Phys.*, 1999, **1**, 5717–5724.

57 C. Li, K. Domen, K.-I. Maruya, T. Onishi, *J. Catal.*, 1990, **125**, 445–455.

58 F. Ouyang, J. N. Kondo, K.-I. Maruya, K. Domen, *J. Phys. Chem. B*, 1997, **101**, 4867–4869.

59 G. N. Vayssilov, M. Mihaylov, P. St. Petkov, K. I. Hadjiivanov, K. M. Neyman, *J. Phys. Chem. C*, 2011, **115**, 23435–23454.